

Influence of boundary conditions on non-equilibrium heat transport under ultrafast laser action based on the lattice Boltzmann method

Yudong Mao ^{*}, Shouyu Liu, Jiying Liu, Mingzhi Yu, Xinwei Li, Kaimin Yang

School of Thermal Engineering, Shandong Jianzhu University, Jinan, 250101, China



ARTICLE INFO

Handling Editor: Dr Y Su

Keywords:
Non-equilibrium heat transport
Boundary conditions
Ultrafast laser
Size effect
Lattice Boltzmann method

ABSTRACT

Based on the lattice Boltzmann method, this paper simulated the non-equilibrium heat transfer process in nano-silicon thin film under ultrafast laser irradiation. The influence of boundary conditions on heat transport was investigated. Results show that under rebound and diffuse boundary conditions, the energy distribution within the film is non-uniform due to interface effects. However, the specular boundary condition is equivalent to eliminating the interface, resulting in a smooth energy distribution. Under convective boundary conditions, the thermal wave phenomenon disappears owing to the open interface. When the energy tends to be stable, the energy density under convective boundary conditions is reduced to 50% of that under adiabatic boundary conditions. As the film size decreases, the differences between boundary conditions become more significant. Particularly when the film size is smaller than the phonon mean free path, the influence of boundary conditions cannot be neglected. Therefore, boundary conditions and size effects are important for the design of nanodevices. Furthermore, compared with the results obtained by the Cattaneo-Vernotte model, it is found that at smaller Knudsen numbers, the Cattaneo-Vernotte model has a better match with the lattice Boltzmann method.

1. Introduction

As the field of microelectronics and semiconductor devices transitions to the nanoscale [1], the development of ultrafast laser technology has emerged as an indispensable tool for thermal treatment of micro/nano devices [2]. Ultrafast laser heating of nanodevices has found widespread applications in cutting-edge fields such as photovoltaic material processing [3], integrated photonic chips [4], and energy conversion [5]. However, this heating process is often accompanied by non-equilibrium heat transport [6]. Particularly, as the semiconductor size shrinks to the order of the phonon mean free path, phonon boundary scattering becomes dominant while intrinsic phonon scattering is suppressed, making boundary conditions a crucial factor affecting non-equilibrium thermal transport [7,8].

The interaction between ultrafast lasers and micro/nano devices is intricate [9,10]. The ultrafast response time of ultrafast lasers and the ultra-small size of nanodevices render the continuity assumption [11] and the classical Fourier's law [12,13] inadequate. The Cattaneo-Vernotte (CV) model, which accounts for the relaxation time between heat flux and temperature gradient, enables the description of non-Fourier effects in non-equilibrium states [14,15]. Belmabrouk et al. [16] have utilized the phonon Boltzmann transport equation (BTE) to derive ballistic-diffusive equations and the CV model, investigating thermal conduction across multiple

* Corresponding author.

E-mail address: maoyudong@sdjzu.edu.cn (Y. Mao).

interfaces in silicon nano-layers. Tzou [17] introduced the dual-phase lag (DPL) model, rooted in a generalized notion of heat flux vector and temperature gradient, to macroscopically delineate microscopic thermal conduction in materials [18]. Yuvaraj and Senthil Kumar's comparative study [19] of diffusion, thermal wave, and DPL conduction modes underscored the finite speed of thermal conduction in the CV and DPL models, contrasting the infinite speed posited by the Fourier diffusion paradigm. However, the CV and DPL models, as modifications of the traditional Fourier's law, are essentially phenomenological. Despite their utility in characterizing thermal conduction within specified domains, they lack an inherent physical rationale based on molecular interactions [20].

To elucidate particle motion and behaviors at the molecular level, numerical methodologies such as the BTE [21], molecular dynamics (MD) [22], and Monte Carlo (MC) [23] simulations have been widely adopted. Among these, the Lattice Boltzmann Method (LBM) [8,11,24] stands out as a prevalent numerical solution to the BTE, adept at simulating particle transport processes by delineating the discrete directional distribution of particles across time and space. The LBM transcends traditional continuum models by offering expeditious computation and streamlined, intuitive handling of boundary conditions, thereby accurately capturing the impacts of boundary conditions [25]. The D2Q5 and D2Q9 lattices are often used in 2D nanoscale heat transfer simulations [26,27]. Li et al. [28] revealed that the D2Q9 lattice enhances simulation accuracy, offering second-order precision in boundary treatment for straight wall conditions, surpassing the first-order accuracy provided by D2Q5. Moreover, Hammer et al. [29] highlighted that in-plane heat transfer problems under adiabatic diffusion boundary conditions require LBM schemes with more propagation directions to accurately describe physical processes. Consequently, the D2Q9 lattice, with its extensive discrete velocity directions, though slightly increasing computational demands, more precisely captures isotropic particle movement.

In nanomaterials, different boundary conditions can be examined by changing the feature size, thereby elucidating the contributions of various scattering mechanisms [30]. Phonon confinement impacts the thermal conductivity of nanowires, with boundary scattering emerging as the dominant factor reducing conductivity as the nanowire thickness increases [31]. Phonon boundary scattering, at the nanoscale, reveals a pronounced size-dependency relative to device dimensions. Han and Liu [32], using the D2Q9 model to study phonon heat transfer across silicon materials with varied cross-sections, demonstrated intensified phonon boundary scattering with decreasing characteristic sizes. Amrit et al. [33] highlighted the non-monotonic relationship between the heat flux, thermal conductivity, and sample size for two-dimensional samples, driven by phonon-phonon interactions surpassing the sample size. The bounce-back scheme, widely employed for solid walls to address no-slip conditions at zero wall velocity. Additionally, the diffuse reflection and specular reflection can effectively replicate ideal adiabatic reflection boundary conditions [34,35]. Gadre et al. [36] experimentally observed non-equilibrium phonons that exist only near the interface, and further developed a novel technique for differential mapping of phonon momentum, directly demonstrating that the interaction between diffuse and specular reflection depends largely on the detailed atomic structure. Shao et al. [37] found that rough surfaces enhance diffusive reflection due to surface irregularities and the presence of Rayleigh waves, whereas fixed surface edges can selectively mitigate these waves, boosting the specular reflection ratio and, consequently, increasing the material's effective thermal conductivity.

In summary, as devices shrink to the nanoscale, boundary conditions emerge as pivotal factors influencing non-equilibrium heat transfer [36–38]. However, a comprehensive comparative study on the impact of boundary conditions is still lacking. Addressing this gap, the LBM was employed to scrutinize the influence of three adiabatic (specular, rebound and diffusive) and convective boundary conditions on heat transport, analyzing thermal transport behavior from diffusive to ballistic regimes under size effects. Furthermore, a comparison between LBM simulation results and the analytical CV model was conducted, shedding light on the disparities between non-Fourier thermal models and numerical approaches.

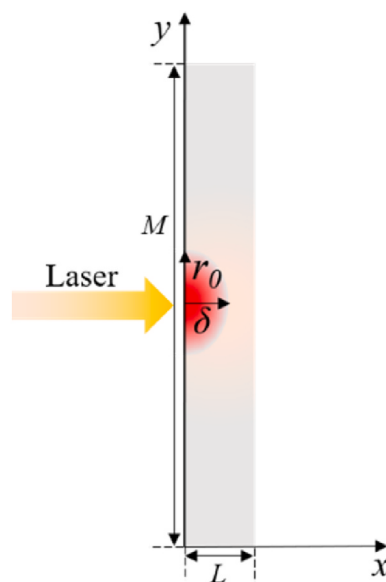


Fig. 1. Physical model of ultrafast laser irradiation of nano-thin films.

2. Mathematical analysis

2.1. Physical model

A two-dimensional nano-silicon film with four boundaries is selected as a case study. As shown in Fig. 1, the ultrafast laser is irradiated vertically from the left center of the film. The influence radius of the ultrafast laser is denoted as r_0 , and the longitudinal penetration depth is represented as δ . The thickness of the film is L , while the radial size M is proportional to the thickness, with a value ten times that of L .

2.2. Application of LBM in the physical model

The LBM significantly reduces computational load for BTE by employing the single-time relaxation Bhatnagar- Gross-Krook (BGK) collision model [11], which can be expressed as [25,26]:

$$\frac{\partial f}{\partial t} + \nu \cdot \nabla f = \frac{f^{eq} - f}{\tau} \quad (1)$$

where f is the distribution function of the hot carrier, t is the time variable, f^{eq} is the equilibrium distribution function, ν is the group velocity of the hot carrier, and τ is the relaxation time of the hot carrier.

The D2Q9 lattice can effectively simulate the two-dimensional heat transfer problem. In semiconductor silicon, phonons are the main hot carriers. In the absence of external forces, the governing equation for phonon energy density can be articulated as follows [28]:

$$\frac{\partial \theta_i}{\partial t} + \nu_i \left(\frac{\partial \theta_i}{\partial x} + \frac{\partial \theta_i}{\partial y} \right) = - \frac{\theta_i - \theta_i^0}{\tau} \quad (2)$$

where i represents the discrete velocity index of the D2Q9 lattice, ranging from 0 to 8. θ represents the energy density of phonons, θ^0 denotes the equilibrium energy density, x and y are the positional parameters. To simplify the calculations, the following dimensionless parameters are introduced:

$$x^* = x/L, y^* = y/L, t^* = t/\tau \quad (3)$$

$$\varphi_0 = \theta(T_0) = C_v T_0 \quad (4)$$

$$\theta_i^* (x^*, y^*, t^*) = \frac{\theta_i(x, y, t) - \omega_i \varphi_0}{\varphi_0} \quad (5)$$

$$\theta^* = \sum_0^8 \theta_i^* = \frac{\theta(x, y, t) - \varphi_0}{\varphi_0} \quad (6)$$

where x^* and y^* are dimensionless position, t^* is dimensionless time, φ_0 is the energy at the initial temperature T_0 , C_v is the volumetric heat capacity of silicon. θ^* is the total dimensionless energy density, θ_i^* represents dimensionless energy density along different discrete directions, ω_i is the weight coefficient.

The absorption rate of laser energy $G(x, y, t)$ is expressed as:

$$G(x, y, t) = 0.94J \frac{1-R}{tp \cdot \delta} \exp \left(-\frac{x}{\delta} - \frac{y^2}{r_0^2} - 1.992 \frac{t}{tp} \right) \quad (7)$$

where J is the laser energy density, R is surface reflectance, t_p is the duration of the laser pulse, r_0 and δ are introduced in Section 2.1.

By combining Eq. (7) with Eq. (2), the governing equation can be derived:

$$\frac{\partial \theta_i}{\partial t} + \nu_i \left(\frac{\partial \theta_i}{\partial x} + \frac{\partial \theta_i}{\partial y} \right) = - \frac{\theta_i - \theta_i^0}{\tau} + G(x, y, t) \quad (8)$$

Then, substituting Eqs. (3)–(6) into Eq. (8), the dimensionless governing equations are obtained:

$$\frac{\partial \theta_0^*}{\partial t^*} = \frac{4\theta^*}{9} - \theta_0^* + \frac{4G_0\gamma}{9\varphi_0} \exp(-\xi x^* - \varepsilon^2 y^{*2} - 1.992at^*) \quad (9)$$

$$\frac{\partial \theta_1^*}{\partial t^*} + Kn \frac{\partial \theta_1^*}{\partial x^*} = \frac{\theta^*}{9} - \theta_1^* + \frac{G_0\gamma}{9\varphi_0} \exp(-\xi x^* - \varepsilon^2 y^{*2} - 1.992at^*) \quad (10)$$

$$\frac{\partial \theta_2^*}{\partial t^*} - Kn \frac{\partial \theta_2^*}{\partial x^*} = \frac{\theta^*}{9} - \theta_2^* + \frac{G_0\gamma}{9\varphi_0} \exp(-\xi x^* - \varepsilon^2 y^{*2} - 1.992at^*) \quad (11)$$

$$\frac{\partial \theta_3^*}{\partial t^*} + Kn \frac{\partial \theta_3^*}{\partial y^*} = \frac{\theta^*}{9} - \theta_3^* + \frac{G_0 \gamma}{9 \varphi_0} \exp(-\xi x^* - \varepsilon^2 y^{*2} - 1.992 a t^*) \quad (12)$$

$$\frac{\partial \theta_4^*}{\partial t^*} - Kn \frac{\partial \theta_4^*}{\partial y^*} = \frac{\theta^*}{9} - \theta_4^* + \frac{G_0 \gamma}{9 \varphi_0} \exp(-\xi x^* - \varepsilon^2 y^{*2} - 1.992 a t^*) \quad (13)$$

$$\frac{\partial \theta_5^*}{\partial t^*} + Kn \left(\frac{\partial \theta_5^*}{\partial x^*} + \frac{\partial \theta_5^*}{\partial y^*} \right) = \frac{\theta^*}{36} - \theta_5^* + \frac{G_0 \gamma}{36 \varphi_0} \exp(-\xi x^* - \varepsilon^2 y^{*2} - 1.992 a t^*) \quad (14)$$

$$\frac{\partial \theta_6^*}{\partial t^*} - Kn \left(\frac{\partial \theta_6^*}{\partial x^*} + \frac{\partial \theta_6^*}{\partial y^*} \right) = \frac{\theta^*}{36} - \theta_6^* + \frac{G_0 \gamma}{36 \varphi_0} \exp(-\xi x^* - \varepsilon^2 y^{*2} - 1.992 a t^*) \quad (15)$$

$$\frac{\partial \theta_7^*}{\partial t^*} + Kn \left(\frac{\partial \theta_7^*}{\partial x^*} + \frac{\partial \theta_7^*}{\partial y^*} \right) = \frac{\theta^*}{36} - \theta_7^* + \frac{G_0 \gamma}{36 \varphi_0} \exp(-\xi x^* - \varepsilon^2 y^{*2} - 1.992 a t^*) \quad (16)$$

$$\frac{\partial \theta_8^*}{\partial t^*} - Kn \left(\frac{\partial \theta_8^*}{\partial x^*} + \frac{\partial \theta_8^*}{\partial y^*} \right) = \frac{\theta^*}{36} - \theta_8^* + \frac{G_0 \gamma}{36 \varphi_0} \exp(-\xi x^* - \varepsilon^2 y^{*2} - 1.992 a t^*) \quad (17)$$

$$G_0 = 0.94J(1-R)/\delta, \xi = L/\delta, \varepsilon = L/r_0, a = \tau/tp \quad (18)$$

where $Kn = \Lambda/L$, represents the Knudsen number, Λ is the mean free path of phonons. G_0 , ξ , ε and a are the transition parameters with no special meaning. After discretizing the dimensionless governing equations and neglecting higher-order terms, numerical simulations can be performed.

2.3. Boundary conditions

2.3.1. Adiabatic boundary conditions

This section introduces three distinct adiabatic boundary conditions that are applied to the D2Q9 lattice. Fig. 2 illustrates the reflection mode for the left boundary, while the other three boundaries follow a similar mode, thus their details are not explicitly described. The dashed lines represent phonons that collide with the boundary, while solid lines of the same color represent phonons that are reflected back into the domain.

Under the specular boundary condition, as depicted in Fig. 2(a), when particles collide with the boundary, they reflect back into the domain with the same tangential velocity as before the collision. This behavior effectively simulates the absence of boundary, as the velocity of particles remains unchanged [8]. Specular boundary conditions are suitable for modeling smooth walls and can simulate free-sliding fluid-solid boundaries.

The left boundary condition is as follows:

$$f1(1,j,k) = f2(2,j,k), f5(1,j,k) = f6(2,j-1,k), f8(1,j,k) = f7(2,j+1,k) \quad (19)$$

where the notation $f_i = {}_{0-8}(u,j,k)$ represents the distribution function of phonons, u represents the discrete direction node in the x direction, j represents the discrete direction node in the y direction, k represents the discrete time node.

Fig. 2(b) illustrates the rebound boundary condition, where a particle hitting the boundary bounces back or reflects completely, resulting in a reversal of its direction. This causes the particle to move in the opposite direction upon contact with the boundary. Therefore, if the velocity component at the wall is zero, a rebound scheme is typically used to simulate a non-slip wall.

The left boundary condition is as follows:

$$f1(1,j,k) = f2(2,j,k), f5(1,j,k) = f7(1,j,k), f8(1,j,k) = f6(1,j,k) \quad (20)$$

As shown in Fig. 2(c), under the diffuse reflection boundary condition, the particle scatters in a random direction upon contacting

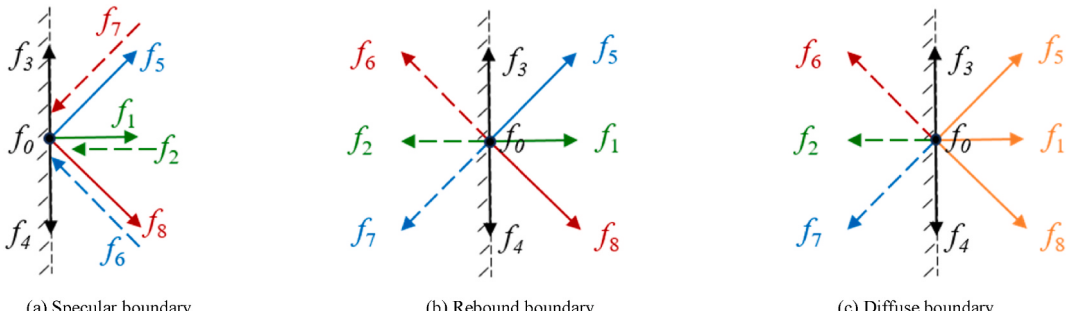


Fig. 2. Adiabatic boundary conditions in D2Q9 lattice.

the boundary. This behavior causes the particles to move more randomly near the boundary [8], leading to the redistribution of energy at the boundary. This boundary condition is often used to model rough surfaces or boundaries with microscopic irregularities.

The left boundary condition is as follows:

$$f1, 5, 8(1, j, k) = [f2(1, j, k) + f6(1, j, k) + f7(1, j, k)]/3 \quad (21)$$

2.3.2. Convection boundary condition

During the processing of thin films, they are usually exposed to air in many cases, so it is more realistic to choose convective boundary conditions [39]. Therefore, we investigate the difference between convective boundary conditions and adiabatic boundary conditions. Due to the limitation of the size of the film and the laser heat source, we adopted a simplified method by setting the right boundary of the film as the convection boundary condition. The other three boundaries of the film are maintained as mirror boundary conditions.

Under the convective boundary condition, the air temperature T_f outside the film is assumed to be 300K, the convective heat transfer coefficient h is 200W/(m².K) [40]. The governing equation is as follows:

$$-K_{eff} \frac{\partial T}{\partial x} = h(T - T_f) \quad (22)$$

where T is the temperature of the film, K_{eff} is an equivalent thermal conductivity that can reflect the size effect [41]:

$$K_{eff} = \frac{K_{bulk}}{2\pi^2 Kn^2} \left[\sqrt{1 + 4\pi^2 Kn^2} - 1 \right] \quad (23)$$

where K_{bulk} is the bulk thermal conductivity of silicon.

After discretizing the dimensionless governing equation and neglecting the higher-order terms, the convection boundary conditions on the right side of the film can be expressed as follows:

$$f2(m, j, k) = f2(m - 1, j, k) - \frac{\Delta x h L}{K_{eff}} f2(m, j, k - 1) \quad (24)$$

$$f6(m, j, k) = f6(m - 1, j, k) - \frac{\Delta x h L}{K_{eff}} f6(m, j, k - 1) \quad (25)$$

$$f7(m, j, k) = f7(m - 1, j, k) - \frac{\Delta x h L}{K_{eff}} f7(m, j, k - 1) \quad (26)$$

where m denotes the discrete node at the right boundary, Δx represents the spatial step size.

2.4. Application of CV model in the physical model

The CV model is utilized to address the same problem mentioned above in order to investigate the differences between the non-Fourier model and LBM. In the CV model, the specular adiabatic boundary condition is implemented, and the dimensionless variation is maintained consistent with LBM.

By combining the CV heat conduction model [14,15] with the energy conservation equation, the governing equation for temperature in the problem can be derived:

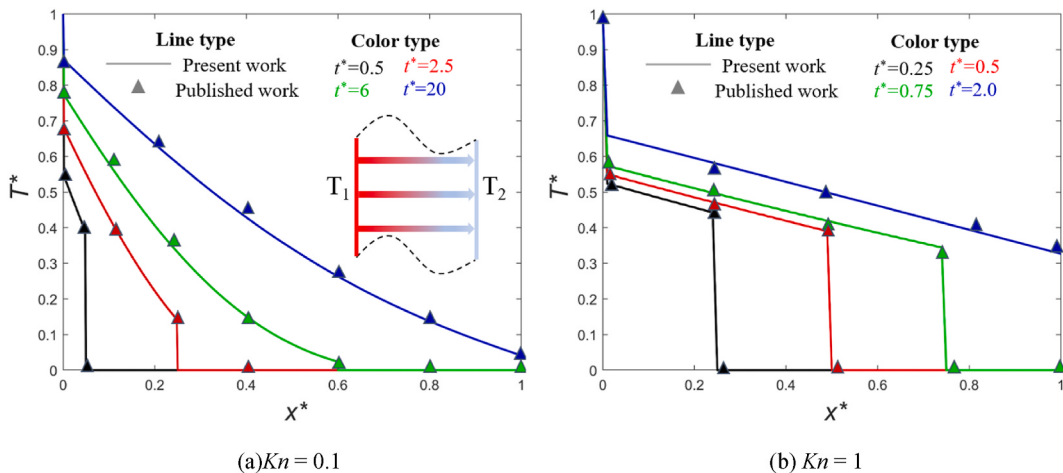


Fig. 3. Validation of present work with Ref. [24].

$$a \frac{\partial^2 T^*(y^*, x^*, t^*)}{\partial t^{*2}} + \frac{\partial T^*(y^*, x^*, t^*)}{\partial t^*} = \frac{K_{bulk} t_p}{C_v} \left(\frac{1}{M^2} \left(\frac{\partial^2 T(y^*, x^*, t^*)}{\partial y^{*2}} + \frac{\partial T(y^*, x^*, t^*)}{y^* \partial y^*} \right) + \frac{\partial^2 T(y^*, x^*, t^*)}{L^2 \partial x^{*2}} \right) + \frac{(1 - 1.992a) G_0 Q^*(y^*, x^*, t^*)}{C_v T_0} \quad (27)$$

$$Q^*(y^*, x^*, t^*) = \exp(-\zeta x^* - \varepsilon^{*2} y^{*2} - 1.992t^*) \quad (28)$$

where a represents the ratio of τ to t_p , T is the temperature of the film, T^* is the dimensionless temperature defined as $T^* = T - T_0 / T_0$, where T_0 is the initial temperature.

The integral transformation method is employed to solve Eq. (27). Then, according to the gray model in Debye hypothesis [42], the relation of temperature with phonon energy density can be obtained as $T^* = T_0 \theta^*$.

3. Validation

Conducting comprehensive experiments on these ultra-small and ultra-fast processes is nearly impossible. Therefore, to ensure the accuracy of the numerical calculation methods, the results of present work are compared with published work [24] for validation. A simplified one-dimensional silicon film heat transfer model is established as shown in Fig. 3(a), with the laser heat source removed to consistent with the mathematical model. The dimensionless temperature T^* , is defined as $(T - T_2) / (T_1 - T_2)$, where T_1 represents the hot boundary temperature set at 301 K, and T_2 represents the cold boundary temperature set at 300 K.

The verification results of the heat transfer process under different dimensionless times t^* are shown in Fig. 3. Under the diffusive state ($Kn = 0.1$), the maximum dimensionless temperature error of present work was 5%, while under the transitional state ($Kn = 1$), the maximum error was reduced to 2%. It can be seen that in the transition from the diffusive state to the transitional state, the verification results of present work agreed well with the published work [24], and this quantitative comparison further supported the accuracy of the model.

4. Results and discussion

Table 1 presents the physical parameters of nano-silicon thin films and ultrafast laser. These parameters are utilized in the subsequent calculations unless otherwise specified. The laser pulse duration $t_p = 0.65$ ps, combined with Eq. (2), it can be seen that the laser pulse starts to launch when $t^* = 0$, and ends when $t^* = 1$. In order to show the heat transport process as completely as possible, the transient dimensionless energy density distributions at different dimensionless time t^* are shown in the following results.

The Knudsen number (Kn) plays a vital role in size effects and thermal transport characteristics within thin films. When the value of Kn is around 1, it means that the characteristic size of the thin film is comparable to the mean free path of phonons, which leads to complex non-continuum effects. Therefore, this paper selects three Kn values around $Kn = 1$ (0.5, 1 and 2) as study cases [43]. The heat transfer behavior in this transitional regime is of great research significance.

4.1. Analysis of heat transport process inside the film

The specular boundary condition is employed to examine the heat transport process within the film. As illustrated in Fig. 4, during the laser pulse duration ($t^* < 0.1$), photons emitted by the laser are absorbed by the lattice atoms or ions, triggering phonon excitation and lattice vibrations. This continuous absorption of photons by the film leads to a swift increase in energy density on the left side within a picosecond timeframe. Upon the conclusion of the pulse ($t^* = 0.1$), the photons carried by the laser cease, and the energy density on the left side peaks at a value of 1.94. Subsequently, heat transfer is primarily facilitated by lattice vibrations, driven by temperature differentials.

In the phonon interaction process, energy and momentum are exchanged via phonon-phonon scattering, propagating continuously through the thickness and radial directions of the film. This propagation, unlike traditional equilibrium heat transfer, occurs at a finite speed in non-equilibrium heat transport, resulting in the phenomenon of thermal waves [19], as depicted in Fig. 4. Given the face-centered cubic structure of silicon crystals, thermal waves propagate isotropically within the thin film, allowing for uniform propagation speeds in both thickness and radial directions.

Fig. 4(c) reveals that the thermal wave along the thickness direction has reached the right boundary of the film ($x^* = 1$), whereas the two thermal waves along the radial direction have arrived at dimensionless positions $y^* = 4$ and $y^* = 6$ with $\theta^* = 0.28$. However, the thermal wave peak in the thickness direction is more pronounced, with $\theta^* = 0.62$, indicating that the ultrafast laser imparts more energy along the thickness direction than radially, as outlined in Eq. (6).

Under the specular boundary conditions, the incident phonons undergo a change in propagation direction while conserving the energy, momentum, and frequency. Thus, once the thermal wave reaches the boundary of the film, it reverses direction. By $t^* = 2$, the thermal wave moving along the thickness direction has returned to the left boundary, while the thermal wave propagating along the

Table 1

Physical parameters of nano-silicon thin films and ultrafast laser [43].

$T_0 = 300\text{K}$	$\Lambda = 41\text{ nm}$	$J = 732\text{ J/m}^2$
$K_{bulk} = 148\text{ W/(m}\cdot\text{K)}$	$\tau = 6.5\text{ps}$	$\delta = 15.3\text{ nm}$
$C_v = 2.3 \times 10^6\text{ J/(m}^3\cdot\text{K)}$	$t_p = 0.65\text{ps}$	$R = 0.93$

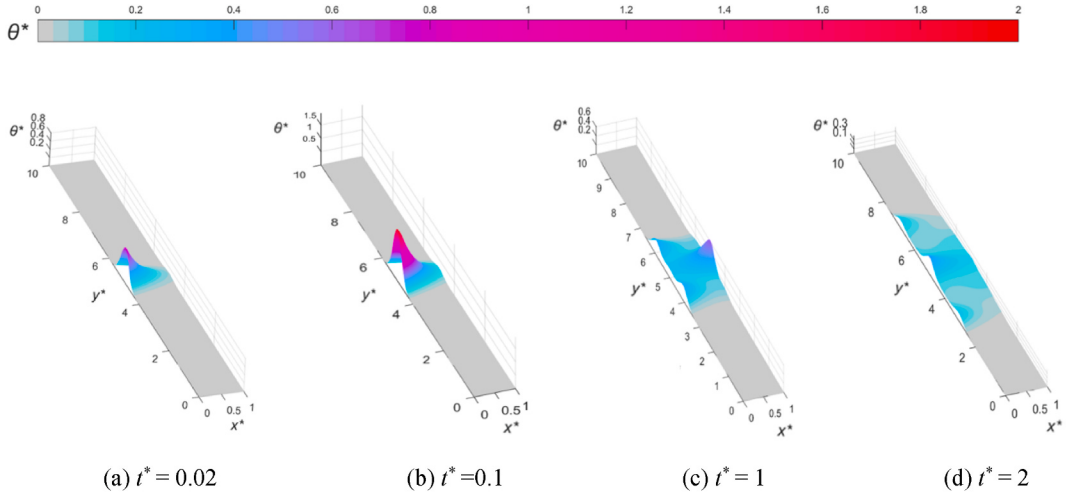


Fig. 4. Cloud diagram of dimensionless energy density distribution inside the film at $Kn = 1$.

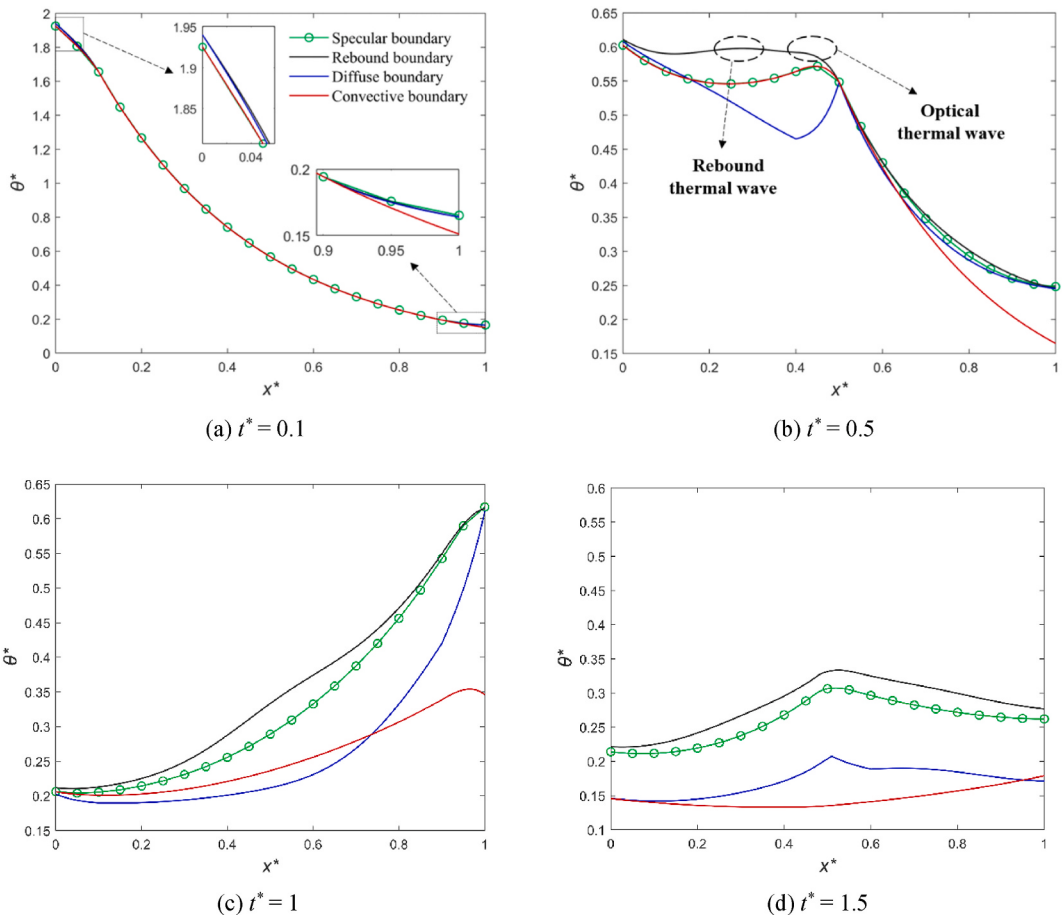


Fig. 5. The transient dimensionless energy density distribution in the tangential direction within the film under different boundary conditions at $Kn = 1$.

radial direction undergoes the same process upon arriving the farther boundary. Throughout this energy transfer phase, the thermal waves continue to oscillate back and forth, with the peak energy density gradually diminishing until equilibrium is achieved.

4.2. Influence of boundary conditions on heat transport process

This section elucidates the impact of the four boundary conditions delineated in Section 2.3 on the heat transfer process within the film, as illustrated in Fig. 5. At $t^* = 0.1$, the energy density at the left boundary attains its maximum, revealing no marked differences among the boundary conditions due to the brief duration of heat transfer at this initial stage. However, as heat propagates through the film, a pronounced thermal wave peak is observed at $x^* = 0.5$ when $t^* = 0.5$. The dimensionless distance traversed by the thermal wave, denoted by $x^* = Knt^*$, depends on the discrete speed intrinsic to the LBM. As time progresses, the effects of the boundary conditions on the energy density distribution within the system become more apparent.

Under the rebound boundary condition, phonons are fully reflected at the boundary, altering their direction and engendering interface scattering. This process retains some energy at the boundaries, with the remainder being re-propagated into the medium through reflected phonons, effectuating an energy redistribution and the emergence of energy waves. Consequently, the rebound boundary condition engenders the appearance of two distinct thermal waves within the film, as depicted in Fig. 5(b). The lagging "second wave" arises from the rebounded phonons emanating from the boundary, culminating in a non-uniform energy distribution. Conversely, the faster-moving thermal wave, generated by photon-excited phonons, propagates independently of the boundary conditions.

The specular boundary condition models an ideally flat and smooth interface, facilitating total phonon reflection without scattering and preserving their propagation trajectory. This characteristic upholds the continuity of phonon transport paths, fostering a more uniform energy distribution across the film. In contrast, the diffuse boundary condition, indicative of increased interface roughness, escalates the probability of phonon scattering. Such scattering disrupts the energy propagation continuum, with a portion of the energy being either scattered or absorbed, thereby hindering efficient energy transfer. This augmented scattering intensifies phonon transport losses, diminishing the effective phonon transport distance [37]. As evidenced in Fig. 5(b)–(d), the average energy density under the diffuse boundary condition is significantly reduced in comparison to that under the other two adiabatic boundary conditions, underscoring the profound influence of phonon-boundary scattering on the thermal behavior within the film.

Contrary to adiabatic boundary conditions that encapsulate the system, convective boundary conditions introduce an open boundary framework, facilitating energy exchange with the external environment. Specifically, the convective boundary condition is applied solely to the right side of the film, resulting in a notable alignment with the specular boundary condition near the left side of the film, as depicted in Fig. 5(b). However, adjacent to the right boundary, there is a continual energy extraction process, where the external fluid dissipates energy away from the film. At this right boundary, the energy density θ^* remains at 0.5 for all adiabatic boundary conditions, contrasting sharply with 0.2 under the convective boundary condition, indicating a substantial reduction in energy density due to convective effects.

Fig. 5(c) and (d) illustrate the growing impact of boundary conditions on internal thermal transport as the heat transfer duration extends. By $t^* = 1$, the thermal wave reaches the right boundary of the film, and under the rebound boundary condition, a distinct "second wave" propagating at a slower pace to $x^* = 0.5$ is also visible. The presence of interface modes generated by both rebound and diffuse boundary conditions introduces additional scattering and interference, leading to a disruption in smooth phonon transport. At $t^* = 1.5$, under adiabatic boundary conditions, the thermal wave attains the dimensionless position $x^* = 0.5$, with the three peaks at 0.35, 0.32, and 0.21, respectively. In stark contrast, under the convective boundary condition, the arrival of the thermal wave at the right boundary and the open boundary setting preclude the formation of phonon boundary scattering, culminating in the dissipation of wave-like energy transfer. This observation highlights that convective boundaries provide a unique mechanism for controlling heat dissipation.

Fig. 6 illustrates the energy density distribution across the radial direction on both the left and right sides of the film at $t^* = 1.5$,

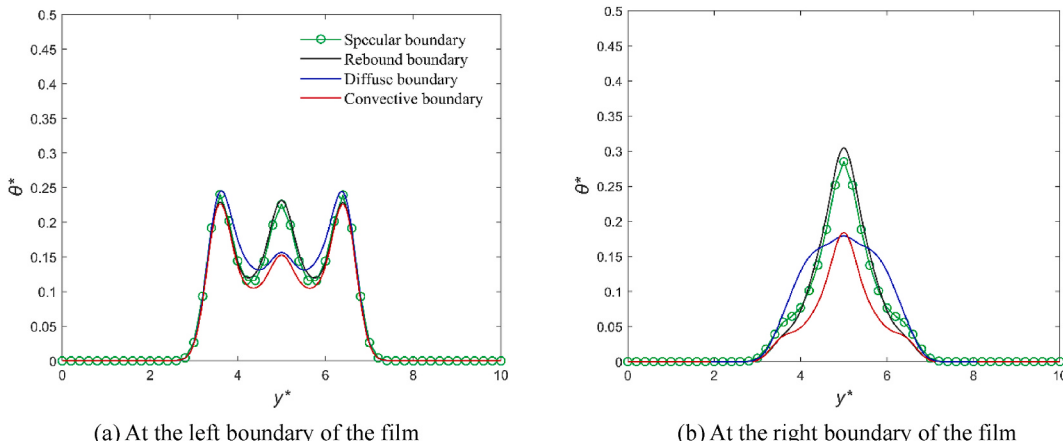


Fig. 6. The transient dimensionless energy density distribution in the radial direction inside the film under different boundary conditions at $t^* = 1.5$.

corresponding to Fig. 5(d). On the left side, photon-induced laser action excites two thermal waves. Conversely, on the right side, energy accumulation is insufficient to precipitate pronounced thermal wave phenomena. Despite the radial thermal wave moving at an identical velocity to its tangential counterpart, it fails to reach the boundary owing to the large radial size. This indicates that energy transport within the film is not impeded by radial boundary conditions. Given the isotropic nature of the D2Q9 model, phonons exhibit similar propagation and interaction patterns. Consequently, phonons in tangential and radial directions can reciprocally affect one another, with radial boundary conditions manifesting different outcomes influenced by tangential boundary dynamics.

According to the principle of energy conservation, the total energy remains unaltered under the three adiabatic boundary conditions. As depicted in Fig. 5(d), the diffuse boundary condition is characterized by a diminished energy density along the tangential direction, but it is compensated in the radial direction. For instance, in Fig. 6(a), the apex of the two thermal waves under the diffuse boundary condition reaches 0.245, surpassing the peaks at 0.241 and 0.229 observed under specular and rebound conditions, respectively. Furthermore, in Fig. 6(b), areas near $y^* = 4$ and $y^* = 6$ showcase elevated energy densities.

Illustrated in Fig. 7, after an extended period, the energy density under the adiabatic boundary conditions uniformly converges to 0.04 and stabilizes. This elucidates that during phonon interactions, the combined phonon distribution in both tangential and radial directions facilitates energy conservation across the system. However, under the convective boundary condition, the energy density θ^* dwindles to 0.02 at $t^* = 20$, continuing to decline at a reduced pace until the energy density reaches zero. Moreover, the thermal wave phenomenon is obliterated by the open boundary condition. In contrast, for the adiabatic boundary conditions, the thermal wave peaks upon each arrival at the left boundary of the film for every two dimensionless time intervals.

4.3. Influence of boundary conditions under size effects

In bulk or macroscopic devices, thermal conductivity typically exhibits independence from size. However, as device dimensions shrink below a specific threshold, the heat conduction pathway may become restricted, leading to a reduction in thermal conductivity with diminishing size. This phenomenon underscores the significance of size effects on thermal properties in nanoscale devices [32, 34]. This section delves into three scenarios characterized by Kn of 0.5, 1, and 2, to elucidate the phonon transition from diffusive to ballistic transport mechanisms.

Fig. 8 reveals that an escalation in the Kn corresponds to an amplification in both the wavelength and the propagation distance of the thermal wave. This phenomenon arises due to phonons traveling at a constant velocity v ($v = \Lambda/\tau$) within the film. With the phonon mean free path remaining constant, an upsurge in Kn effectively denotes a reduction in the thickness size of the film, facilitating the rapid transit of long-wavelength phonons across the film.

Illustrated in Fig. 8(a), at $Kn = 0.5$, phonon diffusion transport predominates, with phonon propagation occurring randomly without a distinct direction. Energy is transferred predominantly through phonon-phonon scattering, as well as interactions with lattice defects and impurities, rendering the influence of boundaries on energy distribution relatively minimal.

At $Kn = 1$, the system navigates a transitional states between diffusive and ballistic transport. Phonon-phonon scattering is observed predominantly in the central region, distant from boundaries, whereas boundary scattering becomes markedly significant closer to the boundaries. The thermal wave advances towards the right boundary of the film at $Kn = 1$, culminating in an abundance of phonon-boundary scattering events. This transition stage demonstrates noticeable variances among different boundary conditions, as depicted in Fig. 8(b).

When $Kn = 2$, phonons evolve from the diffusive regime into the ballistic state, where the mean free path of phonons exceeds the characteristic sizes of the film. Within the confines of the nanoscale structure, phonon-phonon scattering becomes substantially reduced, rendering it almost negligible. Longer-wavelength phonons are less effectively scattered by smaller entities due to diffraction, and lattice defects lose their efficacy as scatterers. Consequently, phonon-boundary scattering emerges as the preeminent mechanism affecting internal thermal transport. In Fig. 8(c), under adiabatic boundary conditions, the thermal wave has been influenced by twice boundary conditions and reaches the left side of the film again, thereby amplifying the distinctions among various boundary conditions. Conversely, under convective boundary conditions, the system approaches an equilibrium state.

Fig. 9 underscores that a heightened Kn results in an expanded non-dimensional energy-affected range and an elongation of the thermal wave's wavelength, mirroring the tendencies observed in the tangential direction. It is crucial to acknowledge, however, that

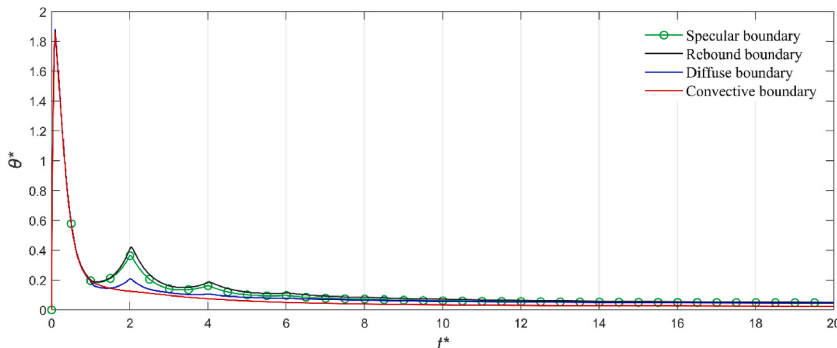


Fig. 7. The dimensionless energy density varies at the point $x^* = 0$ and $y^* = 5$ with dimensionless time under different boundary conditions at $Kn = 1$.

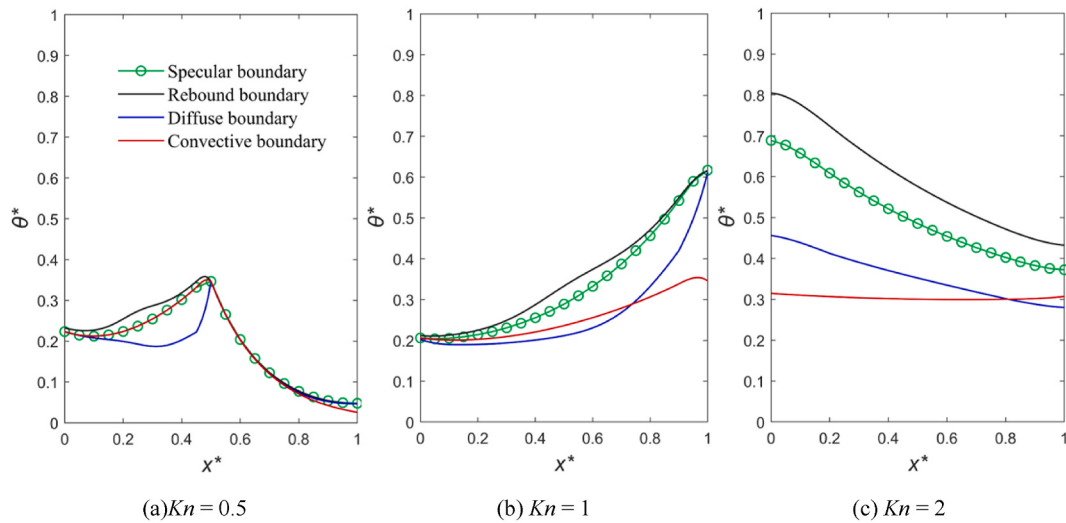


Fig. 8. The dimensionless energy density distribution along the tangential direction under different boundary conditions at $t^* = 1$.

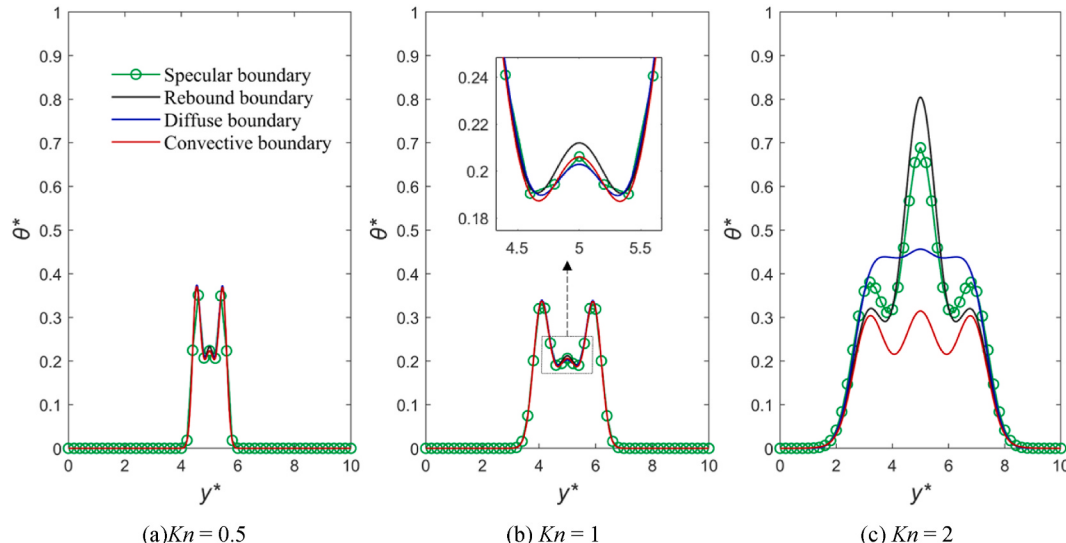


Fig. 9. The dimensionless energy density distribution along the radial direction at the left side of the film under different boundary conditions at $t^* = 1$.

Kn predominantly characterizes the thickness scale rather than the radial scale. Given that the radial dimension is an order of magnitude larger than the thickness. Consequently, within the radial domain, phonons continue to navigate under a diffusive transport regime, with thermal transport heavily influenced by intrinsic phonon scattering, rendering radial boundary conditions relatively inconsequential in this context. While Kn values of 0.5 and 1 exhibit minor disparities among various boundary conditions due to the limited phonon interaction with radial boundaries, the distinctions become markedly pronounced at $Kn = 2$. This is attributed to the tangential thermal wave's reflection back to the left boundary, affecting the radial phonon distribution beyond merely the direct influence of radial boundary conditions.

The above discussion elucidates the critical role of system size in modulating the impact of boundary conditions. In a diffusive regime, boundary conditions exert minimal influence on heat transfer and distribution. Contrastingly, in the ballistic regime, aspects such as scattering, reflection, or interfacial thermal resistance at the boundaries significantly affect thermal conductivity. Thus, both boundary and size effects are of paramount importance in the design of nanomaterials, nano-devices, and other scale-limited systems.

4.4. Comparison of results between CV model and LBM model

The analytical solution of the CV model is compared with the numerical solution derived from the LBM model, as depicted in Figs. 10 and 11. Observations from Fig. 10 indicate that post-laser pulse, the CV and LBM models exhibit analogous trends, yet the peak energy density of 1.75 in the CV model slightly undercuts the 1.94 peak observed in the LBM model. As the heat transfer unfolds, the

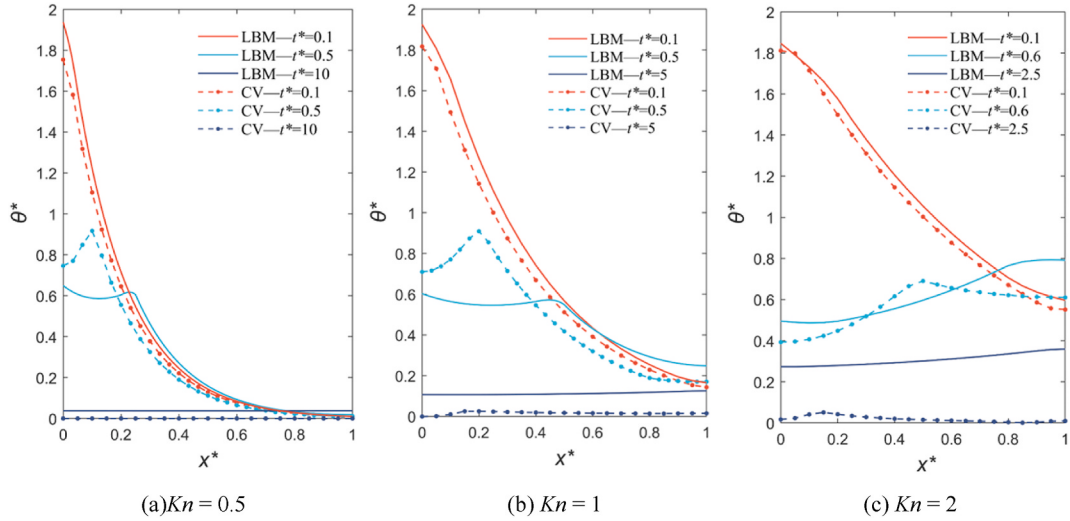


Fig. 10. The transient dimensionless energy density distribution in the tangential direction inside the film with CV model and LBM.

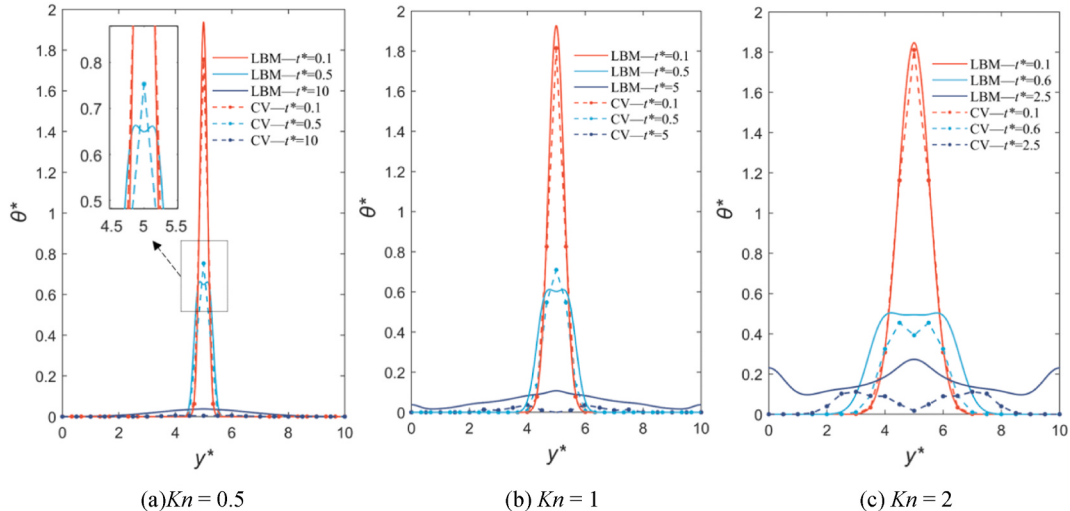


Fig. 11. The transient dimensionless energy density distribution in the radial direction inside the film with CV model and LBM.

delay term intrinsic to the CV model engenders the autonomous emergence and advancement of thermal waves in the presence of a temperature gradient within the film. In this model, the phonon propagation velocity is delineated as $c = Kn/(a\sqrt{3})$, marking a slower pace compared to the LBM model. Nonetheless, Fig. 10(a) reveals a more defined thermal wave in the CV model, with its peak at 0.92 surpassing the 0.61 peak in the LBM model, attributed to the slower propagation speed fostering greater energy consolidation. By $t^* = 10$, the energy within the film approaches equilibrium, with the energy of the CV model asymptotically dwindling to zero. This outcome underscores the tendency of CV model, as an analytical construct, to exhibit more idealized geometrical and boundary conditions, thereby facilitating more efficacious energy transmission avenues.

As the Knudsen number escalates, as illustrated in Fig. 10(a)–(c), phonons evolve from a diffusive to a ballistic regime, hastening their traversal across the film and augmenting the energy density therein. Throughout the equilibrium attainment phase, the CV model precisely delineates the temporal dynamics of thermal conduction, showcasing a relatively accelerated energy dissipation rate. Moreover, both models register an elongation in the thermal wave's wavelength concurrent with rising Kn values. Fig. 10(b) and (c) illustrate that despite minimal energy variations, the CV model retains a wave-like manifestation, whereas, in the LBM outcomes, diminishing differences in phonon energy distribution taper the energy dissipation rate, leading to the gradual fading of the thermal wave phenomenon.

Fig. 11 presents the energy density distribution in the radial direction, complementing the observations from **Fig. 10**. At $t^* = 0.1$, the energy distribution curves of both the CV model and the LBM model closely align, with the exception of a noticeable discrepancy in their peak energy densities. The divergence between the two models is relatively subdued in the radial direction as compared to the

thickness direction. By $t^* = 0.5$, the LBM outcomes already depict faint thermal waves as illustrated in Fig. 11(a) and (b), a phenomenon absent in the CV model results. This discrepancy stems from the inherent delay of CV model, attributing to a more gradual emergence of thermal waves owing to the decelerated speed of phonon movement. As the Kn escalates, as demonstrated in Fig. 11(b)–(c), the extensive radial size further cements the persistence of energy transport within the diffusive regime. Consequently, thermal wave phenomena endure in the radial direction over prolonged durations, distinctively diverging from the tangential direction, particularly in the LBM model.

A compare of Figs. 10 and 11 elucidates that at lower Kn values, the CV model's predictions more closely mirror those of the LBM. However, with an increase in Kn , discrepancies between the CV model's solutions and those of the LBM become more pronounced. This divergence can be attributed to the CV model being a derivative of Fourier's law, which may exhibit limitations in capturing molecular-level interactions in smaller systems [20]. Therefore, the CV model showcases enhanced performance in larger systems, whereas the LBM yields more precise and reliable outcomes for smaller systems. Each model boasts its specific applicability range, necessitating the selection of an appropriate model based on the size effects pertinent to the problem at hand. Specifically for nanoscale challenges, the LBM offers more accurate solutions under non-equilibrium conditions, emphasizing the critical consideration of model choice in the study of thermal dynamics in nanoscale devices.

5. Discussion

The LBM is employed to emphasize the crucial role of boundary conditions in regulating non-equilibrium heat transport. Our observations revealed that temperature distributions under diffuse and specular reflection boundary conditions exhibit markedly different characteristics (either smooth or non-uniform), aligning with the findings reported in Ref. [44]. Intriguingly, we discovered that convective boundary conditions lead to the dissipation of thermal waves, whereas rebound boundaries generate dual thermal waves. Consequently, by fine-tuning the sizes and interfacial microstructures of thin films to suit various boundary conditions, thermal transport properties can be effectively modulated to meet the temperature field requirements essential for crafting specialized functional films. Although our study has explored a multitude of boundary conditions, it primarily scrutinizes idealized scenarios. Practical applications, however, may involve more complex, mixed, or non-uniform boundary conditions. To surmount this limitation, future research should endeavor to investigate more realistic non-ideal boundary conditions, including the study of mixed or non-uniform interfaces and their impact on non-equilibrium thermal transport. Such investigations will significantly bolster our comprehension of thermodynamic behaviors in real-world applications, paving the way for advancements in thermal management technologies.

6. Conclusion

Based on the LBM model, a simulation is carried out to investigate two-dimensional heat transfer in ultrafast laser-irradiated nanoscale silicon thin films. The primary objective is to analyze the influence of boundary conditions on non-equilibrium thermal transport. According to the surface structure of the material, different boundary conditions can be selected, which has a certain reference value for the heat treatment of micro/nano devices. The main conclusions are as follows.

- (1) After laser irradiation, photon excitation induces phonon generation in the film. These phonons propagate at a finite velocity under non-equilibrium conditions, transferring energy within the film as a "thermal wave". With specular boundaries, the thermal waves reflect back and forth between boundaries until reaching equilibrium energy density.
- (2) Under diffusive and rebound boundary conditions, interface effects lead to non-uniform energy distributions inside the film, while specular boundaries exhibit smoother distributions due to the absence of interface effects. For convective boundaries, continuous energy dissipation significantly reduces the energy density compared to adiabatic conditions.
- (3) In adiabatic boundary conditions, energy conservation is maintained through the superposition of radial and tangential distributions. Ultimately, the non-dimensional energy density θ^* approaches 0.04 and remains constant. However, with open convective boundaries, conservation is lost, and θ^* decreases over time, approaching 0.02 when the energy approaches equilibrium.
- (4) As the Kn increases, size effects become more pronounced. Phonon transport transitions from diffusive to ballistic, causing longer thermal wavelengths and faster passage through the film. However, in the ballistic state, boundary scattering dominates heat transport, and the influence of boundary conditions is more significant.
- (5) Compared to the LBM model, the hysteresis effect in the CV model leads to slower thermal wave propagation speeds. However, the energy decreases at a faster rate than in the LBM model, independent of phonon speed. For smaller Kn , the results of the CV model match the LBM results better. While for larger Kn , the LBM can provide more accurate solutions for non-equilibrium heat transport.

CRediT authorship contribution statement

Yudong Mao: Investigation, Methodology, Writing – review & editing. **Shouyu Liu:** Software, Validation, Writing – original draft. **Jiying Liu:** Project administration. **Mingzhi Yu:** Supervision. **Xinwei Li:** Data curation. **Kaimin Yang:** Conceptualization.

Declaration of competing interest

The authors declare that they have no known competing financial interests or personal relationships that could have appeared to influence the work reported in this paper.

Data availability

No data was used for the research described in the article.

Acknowledgements

This work is supported by the Natural Science Foundation of Shandong Province, China (No. ZR2017BEE052), Sub-project of National Key R&D Program (No.2016YFC0700803-01). This work was also supported by the Plan of Introduction and Cultivation for Young Innovative Talents in Colleges and Universities of Shandong Province, and the scientific and technological project of Suzhou City in 2021.

References

- [1] Y.M. Chu, U. Farooq, N.K. Mishra, Z. Ahmad, F. Zulfiqar, S. Yasmin, S.A. Khan, CFD analysis of hybrid nanofluid-based microchannel heat sink for electronic chips cooling: applications in nano-energy thermal devices, *Case Stud. Therm. Eng.* 44 (2023) 102818.
- [2] X. Yang, R.Q. Song, L. He, L.X. Wu, X. He, X.Y. Liu, H. Tang, X.L. Lu, Z.Y. Ma, P. Tian, Optimization mechanism and applications of ultrafast laser machining towards highly designable 3D micro/nano structuring, *RSC Adv.* 12 (2022) 35227–35241.
- [3] H.B. Mo, D. Wang, Q. Chen, W. Guo, S. Maniyarasu, A.G. Thomas, R.J. Curry, L. Li, Z. Liu, Laser-assisted ultrafast fabrication of crystalline Ta-doped TiO₂ for high-humidity-processed perovskite solar cells, *ACS Appl. Mater. Interfaces* 14 (2022) 15141–15153.
- [4] L.Q. Li, W.J. Kong, F. Chen, Femtosecond laser-inscribed optical waveguides in dielectric crystals: a concise review and recent advances, *Adv. Photonics.* 4 (2022) 024002.
- [5] K. Midorikawa, Progress on table-top isolated attosecond light sources, *Nat. Photonics* 16 (2022) 267–278.
- [6] C. Podder, X.T. Gong, H. Pan, Ultrafast, non-equilibrium and transient heating and sintering of nanocrystals for nanoscale metal printing, *Small* 50 (2021) 2103436.
- [7] Y. Hu, S.T. Zhang, Q. He, D. Li, Diffuse interface-lattice Boltzmann modeling for heat and mass transfer with Neumann boundary condition in complex and evolving geometries, *Int. J. Heat Mass Tran.* 215 (2023) 124480.
- [8] A. Nabavati, D.P. Sellan, C.H. Amon, On the lattice Boltzmann method for phonon transport, *J. Comput. Phys.* 230 (2011) 5864–5876.
- [9] B. van de Laar, R. Naus, On the 1D heat equation for laser-medium interaction including convection and radiation at the boundaries, *Int. J. Heat Mass Tran.* 195 (2022) 123171.
- [10] L. Canguiro, J.A. Ramos-de-Campos, D. Bruneel, Prediction of thermal damage upon ultrafast laser ablation of metals, *Molecules* 26 (2021) 6327.
- [11] Y.Y. Guo, M.R. Wang, Lattice Boltzmann modeling of phonon transport, *J. Comput. Phys.* 315 (2016) 1–15.
- [12] R. Baratifarimani, Z. Shomali, Implementation of nonlocal non-Fourier heat transfer for semiconductor nanostructures, *Case Stud. Therm. Eng.* 54 (2024) 104015.
- [13] G. Chen, Non-Fourier phonon heat conduction at the microscale and nanoscale, *Nat. Rev. Phys.* 3 (2021) 555–569.
- [14] B.B. Xu, X.W. Gao, M. Cui, High precision simulation and analysis of non-Fourier heat transfer during laser processing, *Int. J. Heat Mass Tran.* 178 (2021) 121574.
- [15] F. Gamaoun, A. Abdulrahman, G. Sowmya, R. Kumar, U. Khan, A.M. Alotaibi, S.M. Eldin, R.S.V. Kumar, Non-Fourier heat transfer in a moving longitudinal radiative-convective dovetail fin, *Case Stud. Therm. Eng.* 41 (2023) 102623.
- [16] H. Belmabrouk, H. Rezgui, F. Nasri, M.F. Ben Aissa, A.A. Guizani, Interfacial heat transport across multilayer nanofilms in ballistic-diffusive regime, *Eur. Phys. J. Plus.* 135 (2020) 109–117.
- [17] D.Y. Tzou, The generalized lagging response in small-scale and high-rate heating, *Int. J. Heat Mass Tran.* 38 (1995) 3231–3234.
- [18] H.Y. Zhou, P. Li, Dual-phase-lagging thermoelastic damping and frequency shift of micro/nano-ring resonators with rectangular cross-section, *Thin-Walled Struct.* 159 (2021) 107309.
- [19] R. Yuvaraj, D. Senthilkumar, A comparative study of diffusion, thermal wave and dual-phase-lag heat conduction in thin layer, *ISI Bilim Tek Derg* 41 (2021) 101–118.
- [20] M.B. Rubin, Hyperbolic heat conduction and the second law, *Int. J. Eng. Sci.* 30 (1992) 1665–1676.
- [21] J. Chen, X.F. Xu, J. Zhou, B.W. Li, Interfacial thermal resistance: past, present, and future, *Rev. Mod. Phys.* 94 (2022) 025002.
- [22] P. Li, D.L. Feng, Y.H. Feng, et al., Thermal properties of PEG/MOF-5 regularized nanoporous composite phase change materials: a molecular dynamics simulation, *Case Stud. Therm. Eng.* 26 (2021) 101027.
- [23] A.M. Joseph, B.Y. Cao, Electron heat source driven heat transport in GaN at nanoscale: electron-phonon Monte Carlo simulations and a two temperature model, *Materials* 15 (2022) 1651.
- [24] R. Escobar, Lattice Boltzmann Modeling of Phonon Transport in Silicon Films, Carnegie Mellon University, Pittsburgh (PA), 2005.
- [25] Z.X. Tong, M.J. Li, T. Xie, Z.L. Gu, Lattice Boltzmann method for conduction and radiation heat transfer in composite materials, *J. Therm. Sci.* 31 (2022) 777–789.
- [26] H. Kameli, F. Kowsary, Solution of inverse heat conduction problem using the lattice Boltzmann method, *Int. Commun. Heat Mass Tran.* 39 (2012) 1410–1415.
- [27] T. Zhang, D.F. Che, Double MRT thermal lattice Boltzmann simulation for MHD natural convection of nanofluids in an inclined cavity with four square heat sources, *Int. J. Heat Mass Tran.* 94 (2016) 87–100.
- [28] L.K. Li, R.W. Mei, J.F. Klausner, Lattice Boltzmann models for the convection-diffusion equation: D2Q5 vs D2Q9, *Int. J. Heat Mass Tran.* 108 (2017) 41–62.
- [29] R. Hammer, V. Fritz, N. Bedoya-Martinez, The worm-LBM, an algorithm for a high number of propagation directions on a lattice Boltzmann grid: the case of phonon transport, *Int. J. Heat Mass Tran.* 170 (2021) 121030.
- [30] L. Yang, R. Prasher, D.Y. Li, From nanowires to super heat conductors, *J. Appl. Phys.* 130 (2022) 220901.
- [31] K.V. Tretiakov, K. Hyzorek, Role of the phonon confinement effect and boundary scattering in reducing the thermal conductivity of argon nanowire, *J. Chem. Phys.* 154 (2021) 054702.
- [32] Y.F. Han, H.D. Liu, An investigation of phonon heat transport: influence of size and geometric configuration, *J. Comput. Theor. Nanosci.* 12 (2015) 1478–1782.
- [33] J. Amrit, K. Nemchenko, T. Vikhhtinskaya, Effect of diffuse phonon boundary scattering on heat flow, *J. Appl. Phys.* 129 (2021) 085105.
- [34] J.V. Goicochea, M. Madrid, C. Amon, Hierarchical modeling of heat transfer in silicon-based electronic devices, *J Heat Trans-T ASME.* 132 (2010) 1–11.
- [35] J.H. Qian, H.A. Wu, F.C. Wang, A generalized Knudsen theory for gas transport with specular and diffuse reflections, *Nat. Commun.* 14 (2023) 7386.
- [36] C.A. Gadre, X.X. Yan, Q.C. Song, J. Li, L. Gu, H.X. Huyan, T. Aoki, S.W. Lee, G. Chen, R.Q. Wu, X.Q. Pan, Nanoscale imaging of phonon dynamics by electron microscopy, *Nature* 606 (2022) 292–297.
- [37] C. Shao, Q.Y. Rong, N.B. Li, H. Bao, Understanding the mechanism of diffuse phonon scattering at disordered surfaces by atomistic wave-packet investigation, *Phys. Rev. B* 98 (2018) 155418.
- [38] A. Shahzad, F. Liaqat, Z. Ellahi, M. Sohail, M. Ayub, M.R. Ali, Thin film flow and heat transfer of Cu-nanofluids with slip and convective boundary condition over a stretching sheet, *Sci. Rep.* 12 (2022) 14254.
- [39] N. Chen, J.Y. Zhao, J.W. Wei, H. Xiao, L. Li, J.W. Liu, N. Yu, N. He, Influence of laser-processed surfaces on heat transfer performance of microflow channels, *Case Stud. Therm. Eng.* 52 (2023) 103624.
- [40] S.W. Pua, K.S. Ong, K.C. Lai, M.S. Naghavi, Natural and forced convection heat transfer coefficients of various finned heat sinks for miniature electronic systems, *P I MECH ENG A-J POW.* 233 (2019) 249–261.

- [41] F.X. Alvarez, D. Jou, Memory and nonlocal effects in heat transport: from diffusive to ballistic regimes, *Appl. Phys. Lett.* 90 (2007) 083109.
- [42] J.Y. Murthy, S.R. Mathu, An improved computational procedure for sub-micron heat conduction, *J HEAT TRANS-T ASME.* 125 (2003) 904–910.
- [43] Y.D. Mao, M.T. Xu, Lattice Boltzmann numerical analysis of heat transfer in nano-scale silicon films induced by ultra-fast laser heating, *Int. J. Therm. Sci.* 89 (2015) 210–221.
- [44] G.H. Su, Z.C. Yang, F.R. Sun, Modeling the phonon transport in nanowire with different cross-section, *Appl. Mech. Mater.* 401 (2023) 852–855.